 doi:10.20944/preprints202201.0434.v1

,,

Preprints (www.preprints.org) | NOT PEER-REVIEWED | Posted: 28 January 2022 doi:10.20944/preprints202201.0434.v1

Article

Permanently installed Terrestrial Laser Scanner and Synthetic Aperture Radar data: evaluation of correlation factor through time series analysis on coastal area under varying environmental conditions

Valeria Di Biase [1]*, Mieke Kuschnerus [2] and Roderik C. Lindenbergh [3]

[1] Delft University of Technology, 2628 CN, Delft, The Netherlands; v.dibiase@tudelft.nl
[2] Delft University of Technology, 2628 CN, Delft, The Netherlands; m.kuschnerus@tudelft.nl
[3] Delft University of Technology, 2628 CN, Delft, The Netherlands; r.c.lindenbergh@tudelft.nl
* Correspondence: v.dibiase@tudelft.nl

Abstract: In the past years, our knowledge of coastal environments has been enriched by remotely sensed data. However, to successfully extract information from a combination of different sensors systems, it should be understood how these interact with the common coastal environment. In this research we co-analyze two sensor systems: Terrestrial Laser Scanning (TLS) and satellite based Synthetic Aperture Radar (SAR). TLS shows large potential for examining coastal processes thanks to the possibility to retrieve repeated, accurate and dense topographic information in a rapid and non-invasive manner. However, TLS presents some limits due to its high economic costs and limited field of view. SAR systems are among the most used active remote sensor system for Earth Observation. Despite their relatively low resolution, SAR systems provide the ability to monitor and map coastal areas with complete, repeated and frequent coverage, penetrating through clouds and providing all weather monitoring. Moreover, Sentinel-1 SAR images are freely available. The availability of a permanently installed TLS system (PLS, Permanent Laser Scanner) allows us, to extensively compare Sentinel-1 SAR data and topographic laser scans during different conditions on a sandy beach. PLS data are compared with simultaneous Sentinel-1 SAR images in order to investigate the combined use of PLS and SAR in coastal environments. The purpose of this comparison is the investigation of a possible relation between PLS and SAR data: knowing their relation, SAR dataset could be correlated to beaches characteristics. Meteorological and surface roughness have also been taken into consideration in the evaluation of the correlation between PLS and SAR data. The permanently installed laser scanner for the present study is located in Noordwijk (the Netherlands). A generally positive but low correlation exists between the two variables. When considering weather phenomena, their correlation increases and shows a dependence on wind directions and speed. The correlation with the surface roughness, evaluated in terms of root-mean squared height, also depends on specific wind speed and directions.

Keywords: Terrestrial Laser Scanner; SAR; coastal environment; weather effect; surface roughness.

1. Introduction

During the last years, Terrestrial Laser Scanning (TLS) has been successfully exploited in many applications thanks to its ability to capture both geometric information and to register backscatterd laser intensity of the scanned objects. Among its applications, forestry [1–3], river systems [4, 5] and geomorphology [6, 7] have been investigated. In the past years, the knowledge on coastal environments has been enriched by information provided by TLS systems which show significant potential for examining coastal processes [8–10]. Among the coastal applications, TLS have been used in order to generate Digital Elevation Models (DEM) and to evaluate accurate volumetric changes on beaches, dunes and cliffs, [11]: thanks to the high density of the point clouds with high accuracy/precision, TLSs

 doi:10.20944/preprints202201.0434.v1

are suitable for the detailed DEM mapping of features on hundreds of meters of the beach-dunes systems [12]. Several studies have also demonstrated the potential of estimating other beach features as the surface moisture using both short and long-range TLS [10, 13–16].

TLSs have the advantage over other surveying techniques that they can provide accurate and dense information in a rapid and non-invasive manner [17]. Moreover, they can scan a beach repeatedly without correction for changes in illumination because it works as an active sensor [13–15, 18]. On the other hand, TLS has some disadvantages when used in large environments as coastal areas, such as a limited field of view, high economic cost, heavy material (difficulties for portability), longer measurement time, problems with little misalignments requiring calibration of reference points, and sight shadowing [19].

Space-born remote sensing provides a unique ability to monitor and map coastal areas with complete, repeated, and frequent coverage of the Earth's surface, [20]. In particular active microwave remote sensing systems, despite their lower resolution, can penetrate through clouds and provide continuous and all-weather monitoring. This allows for more reliable and consistent sand monitoring. Synthetic Aperture Radar (SAR) is the most common active remote sensing system for Earth observation [21]. In recent years, many studies demonstrated the advantage of using SAR for the estimation of soil surface characteristics, such as surface roughness and soil moisture [22, 23]. Different sensor configurations, in terms of wavelength, polarization, and incidence angle, allow for the discrimination of various soil parameters, such as surface roughness, soil dielectric constant, and vegetation cover [24, 25].

The combined use of TLS and SAR systems has been poorly investigated, and literature is mostly limited to forest fire [26, 27] and vegetation [28] estimation. In this work we present new results from a Permanent terrestrial Laser Scanner (PLS) [29] based investigation on beach environments. Both geometric information and backscatter laser intensity have been collected from a permanently installed laser scanning device, a Riegl VZ-2000 [30]. The PLS results are compared with simultaneous Sentinel-1 Synthetic Aperture Radar (SAR) images [31] in order to investigate, for the first time, the synchronous use of PLS and radar in beach environments. The purpose of this comparison is showing a possible relation between PLS and SAR data: knowing this relation, SAR data could be correlated to beaches characteristics assessable by PLS.

Several studies showed that remote sensing data on coastal environments is affected by variables such as wind condition and surface roughness. This has been shown independently for both PLS [10, 15, 16] and SAR data where the backscattering behaviour depends on the roughness in relation to the wavelength [32, 33] and is affected by wind speed and direction [34]. Therefore, notably meteorological conditions, in terms of wind speed and direction and rain, and surface roughness, will be taken into consideration in the evaluation of the correlation between PLS and SAR data.

The range for which roughness should be quantified depends on the application. In [35], Lane states that roughness, as a component of topography, must be dealt with implicitly at the scale of inquiry: depending on the specific range of scales, there is a diversity in characterizing and defining the surface roughness. Higher-order roughness representing elevation variations in the field ([36]) has been considered in this work.

Methods for soil roughness assessment involve different strategies, using both contact and non-contact devices.

TLS has been investigated as a technique for two-dimensional sampling of soil heights able to detect elevation differences at mm range with relatively small effort, despite the high equipment costs [37–39]. Assessment of surface roughness is one of the most challenging applications of TLSs [40].

One of the most common parameters applied for surface roughness quantification is the standard deviation in vertical direction from a single mean value (Root-Mean Squared Height, RMSH).

Preprints (www.preprints.org) | NOT PEER-REVIEWED | Posted: 28 January 2022 doi:10.20944/preprints202201.0434.v1

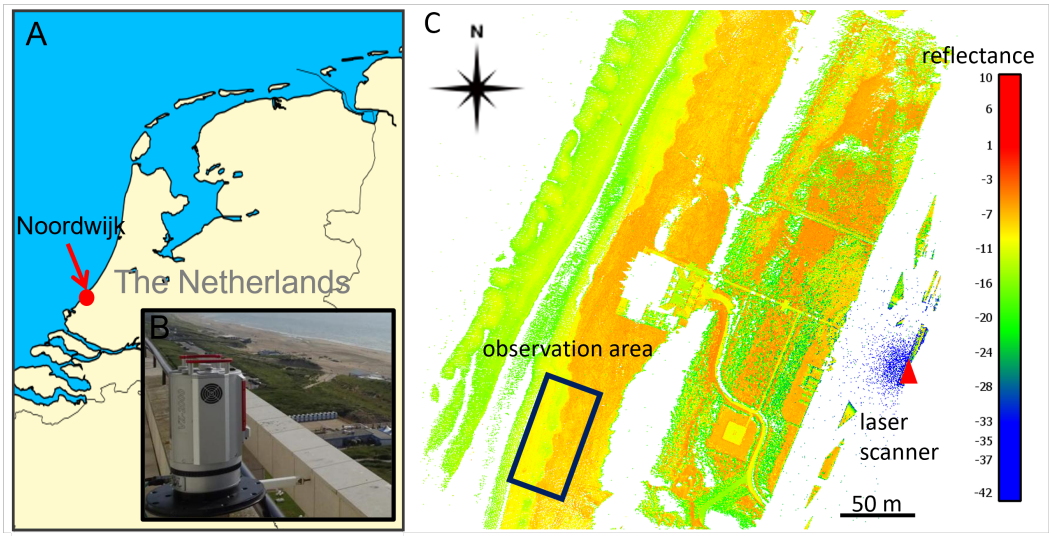

Figure 1. Location of the study site in Noordwijk, The Netherlands (A) with view of the Riegl VZ-2000 laser scanner mounted on the balcony of Grand Hotel Huis ter Duin (B) and point cloud colored with reflection (C) and indication of location of the laser scanner and study site.

Variations in height at different scales affect this index, therefore RMSH values are commonly derived on a previously detrended surface in order to remove the effect of larger scale roughness patterns as slope or curvature and to separate multi-scale effects [41, 42].

In terms of roughness influence on the correlation between SAR and TLS systems, the focus of this paper is to evaluate the effect of the roughness at a decimeter scale resolution on the PLS system and, for the first time, its contribution to the relation between PLS and SAR data. Roughness patterns at different scales were analyzed by RMSH using sliding windows.

After evaluating the RMSH index and considering different weather conditions in terms of wind speed and direction, their contribution has been considered for evaluating to what extent these variables affect the correlation between PLS and SAR dataset.

The paper is structured as follows: in Section 2, the study area, the weather data and the PLS and SAR data sets are presented; in Section 3, the data processing and the roughness evaluation are presented and the methodology used to compare PLS and SAR data is showed; in Section 4, the correlation between SAR and PLS on the study area is presented, followed by the evaluation of the weather and roughness influence. Sections 5 and 6 show the Discussion and Conclusion of the present work.

2. Materials

In this section, the study area and the used weather dataset are described, followed by the presentation of the TLS and SAR data set.

2.1. Study area

The study site consists of a typical urban beach on the Dutch coast in Noordwijk, The Netherlands. It is subject to tidal differences up to 2 m and varies in width between 80 m and 140 m under normal weather conditions. Behind the beach lies a row of dunes. A hotel (Grand Hotel Huis ter Duin) borders the dunes at about 150 m distance from the sandy beach. On the balcony of the top floor of the hotel, at 55 m above sea level, a Riegl VZ-2000 laser scanner was installed to acquire point clouds of the sandy beach and neighbouring dunes every hour for the duration of two years. SAR and PLS data on the study area from the same period ranging 19/08/2019 to 22/04/2021 have been identified. At first, SAR pixels covering the study area have been selected as shown in Figure 2.

Preprints (www.preprints.org) | NOT PEER-REVIEWED | Posted: 28 January 2022 doi:10.20944/preprints202201.0434.v1

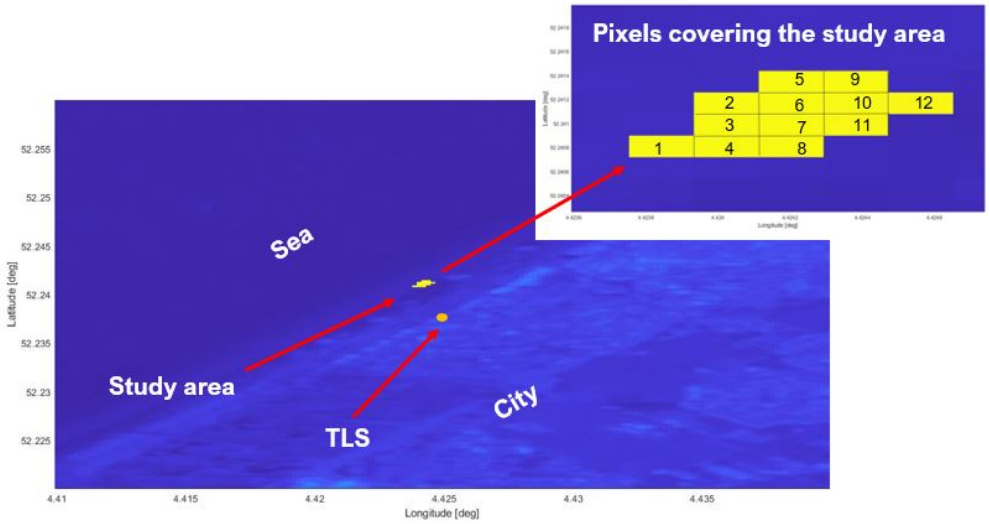

Figure 2. Sentinel-1 image (sigma naught values, VV polarization) from orbit DSC37: the study area is highlighted in yellow and its location is represented with respect to the city, the sea and the PLS position. Top right: the number of the SAR pixels covering the study area.

2.2. Weather dataset

Several meteorological stations monitor the Dutch coast continuously providing detailed variables. Professional weather station data guarantee controlled information but there are no data available close to the study area; therefore in the present study, as a compromise, amateur weather station data have been used. These are less controlled compared to professional weather station data, but available in the area of interest. For the present study, information regarding wind speed and direction and precipitation at the time of the satellite pass were collected. All the weather data used in this study are local information collected at the moment of the satellite pass. Instantaneous values for both wind speed and direction have been used, whilst for the rain the precipitation accumulation, which is the sum of precipitation over a certain period of time, has been used. In particular, the precipitation accumulation over the past 1 hour before the satellite pass has been considered. Three amateur weather stations were selected, since they provide the type of data and the temporal sampling required. The meteorological stations are located in Noordwijk (52.25°N, 4.43°E), Katwijk (N 52.19°N, 4.41°E) and Scheveningen (52.11°N, 4.29°E), all close to beach areas and close to the area of interest (respectively 1 km, 5 km and 15 km). The weather stations in Noordwijk and Scheveningen have high correlation coefficients with each other concerning the wind and rain variables. The wind data set of station Noordwijk during the two years is not as complete as station Scheveningen, therefore it has been discarded. The data set of the station Katwijk has been discarded since the anemometers - devices used for measuring wind speed and direction - are located next to a building or a wall, therefore their correlation with the two other stations was poor. The values of the station Scheveningen have been therefore selected for the present analysis (https://wow.knmi.nl/#919666001s).

Figure 3 shows the scatter of the collected wind speed relatively to the wind direction at the moment of the satellite pass for the selected days of the stack. In the figure, each red dot represents the instantaneous wind value (speed and direction) acquired simultaneously to the Sentinel-1 pass over the study area for the entire stack. Considering the orientation of the coastline, onshore wind occurs for direction ranging $-30°$ and $150°$.

2.3. PLS data set

The selected data consists of point clouds covering an area of approximately 36 m $\times$ 80 m size on the dry part of the beach, which is not covered by tides under normal conditions.

Preprints (www.preprints.org) | NOT PEER-REVIEWED | Posted: 28 January 2022 doi:10.20944/preprints202201.0434.v1

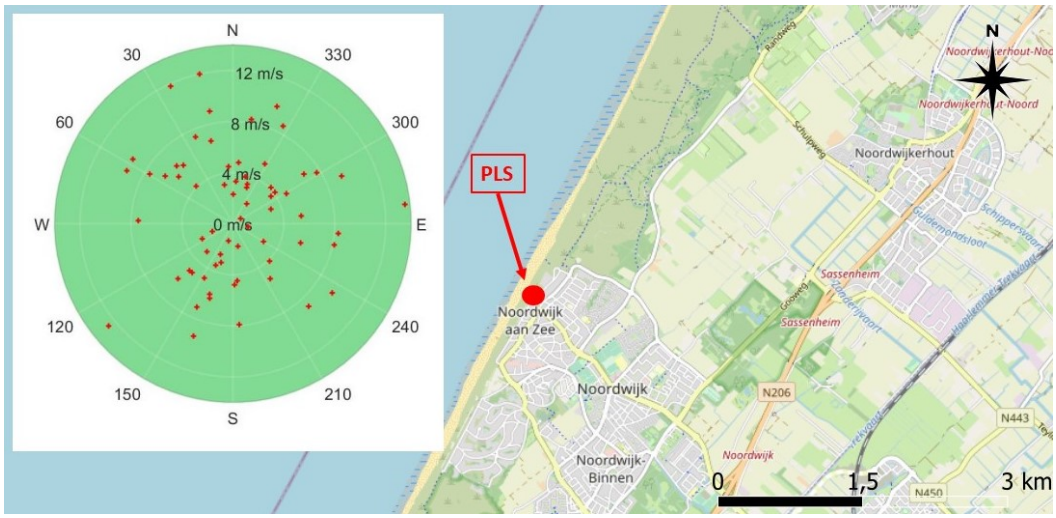

Figure 3. Scatter plot of the local wind direction (0°= North; 90°= East) and wind speed (m/s; represented on the radius) collected during the days of the stack at the moment of the satellite pass. The PLS location is highlighted in red. Background image: QGis.

The data is acquired on the same days and at the same time of the Sentinel-1 pass over the study area. The laser scanner is scanning with 0.03 ° angular resolution (referred to as low resolution - LR - in the following) and at a wavelength of 1550 nm. The study area is at about 250 m range distance and the range accuracy (at 150 m range) equals 0.008 m, according to the specifications [43]. With a slight surface slope of 1 ° towards the sea and away from the laser scanner, the incidence angle is about 77 ° on average. The area contains just under 30 000 points, resulting in a point density of about 10 points per m^2. Because of the relatively large incidence angle and range, the footprint in this area is about 0.066 m^2 with an ellipse shape of 0.3 m diameter on the long side. In the present work, the intensity value is considered for the analysis. The intensity value is normalized with respect to a reference level for each single point, therefore the intensity data is dimensionless [44]. The output have been calibrated to allow the scan data to be range-independent [45].

2.4. SAR data set

Sentinel-1 is a constellation of two Sun-synchronous dawn/dusk orbiting (orbit height: 693 km, platform velocity: about 7.6 km/s) satellites [46], Sentinel-1A and Sentinel-1B, which carry a C-band (operating at a wavelength of about 5 cm wavelenght) SAR sensor. The repeat cycle of the Sentinel-1 constellation is 12 days for the single satellites and six days for the two satellites together. Images at different polarizations and resolutions are collected and free accessible from the Copernicus data hub [47].

For the present study, Sentinel-1 data collected from Google Earth Engine have been used after further processing steps. A single orbit (DSC37, parallel to the Dutch coastline) has been selected. All the available Sentinel-1 images from the orbit DSC37 acquired from 19/8/2019 to 22/4/2021 were downloaded (88 images). In Figure 4 the averaged images in VV and VH polarization during the period of interest are showed. Regarding the polarisation effect, it is well known that HH is more sensitive to surface scattering and VH to volume scattering, and VV a combination of the two. VH backscatter is therefore often used for the retrieval of crop parameters, and HH, ground parameters [48]. Sentinel-1 mission only provides data in VV and VH polarization.

Sentinel-1 imagery in Earth Engine consists of Level-1 Ground Range Detected (GRD). GRD are focused SAR data that have been detected, multi-looked and projected to ground range using an Earth ellipsoid model. The SAR images used in the current study are Interferometric Wide (IW) acquisition mode with 20 × 12 m spatial resolution (range × azimut), dual polarization (VV + VH) and GRD product type. Within this collection, all products have been already preprocessed using the European Space Agency's (ESA)

Preprints (www.preprints.org) | NOT PEER-REVIEWED | Posted: 28 January 2022 doi:10.20944/preprints202201.0434.v1

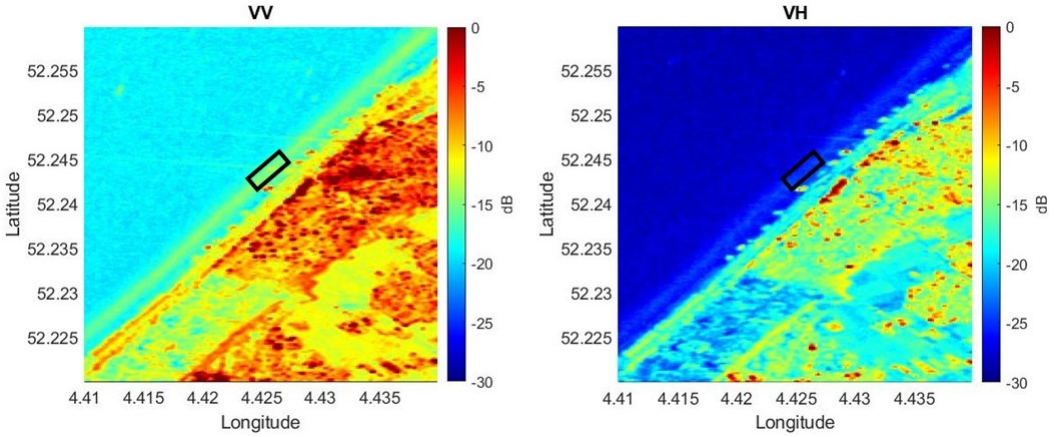

Figure 4. Sentinel-1 images (Left: VV polarization; Right: VH polarization): sigma naught values averaged over the period of interest (19/08/2019 to 22/04/2021) from the orbit DSC37 showing the city of Noordwijk and its coast line with the study area highlighted in the black box.

Sentinel-1 Toolbox (S1TBX), available on the European Space Agency Sentinel-1 Toolbox website [49], with the following steps:

- Step 1: Apply orbit file;
- Step 2: GRD border noise removal;
- Step 3: Thermal noise removal;
- Step 4: Radiometric calibration (calculation of sigma naught values);
- Step 5: Terrain correction (orthorectification).

Once created the stack of images for the area and period of interest, three further steps have been performed:

- Step 6: Normalization of the backscatter coefficients, performed by using a dedicated algorithm. The backscatter of a specific area with a small incidence angle return higher backscatter values than the data of the same area acquired with a higher incidence angle [50];
- Step 7: Cosine correction. It is the most widely used incidence angle correction technique [33];
- Step 8: Noise correction. The images of the Sentinel-1 stack have been cropped including not only the study site but a bigger area also including part of a city in order to perform a noise correction. The pixels with the lowest variability have been evaluated and selected and all the SAR images have been calibrated relatively to the low variability area.

3. Methods

In the present Section, the processing applied to the PLS data in terms of detrending is shown and the methodology to evaluate the roughness index (RMSH) is presented. RMSH is the most common parameter applied in recent studies for quantifying surface roughness [51]. The index is calculated for a regular raster dataset of n $\times$ m pixel values.

3.1. PLS Data processing

After data collection with the Riegl VZ-2000 laser scanner, the individual point clouds are transformed into 3D point clouds in compressed laz-format in a local coordinate system with the projected location of the laser scanner to elevation zero (NAP) as origin. This step is done, in order to obtain positive elevation (NAP) instead of negative values, with respect to the location of the laser scanner at 55 m height. The point clouds are recorded from a fixed location and are therefore already coarsely co-registered (in the order of several centimeters). Fine alignment or geo-location was not deemed necessary for the further analysis for this study. The selected areas of interest are cut out using their x- and y-coordinates and filtered

Preprints (www.preprints.org) | NOT PEER-REVIEWED | Posted: 28 January 2022 doi:10.20944/preprints202201.0434.v1

for outliers, i.e., points which are outside of the expected elevation range (mean elevation of the area with a margin of a few decimeter) for the respective areas. Then a plane is fit through the points representing the selected area using principal component analysis (PCA). With the help of the fitted plane, the slope is calculated and removed from the elevation values of the respective areas, in order to enable the determination of surface roughness, [41].

3.2. RMSH evaluation

Surface roughness is reflected by the spatial heterogeneity of elevation values at a pre-defined scale and its quantification depends on the dimensionality and resolution of the data, as well as on the desired expressiveness of the index [51]. Considering that the PLS provides about 10 cm point spacing at the study area, the roughness scale considered in the present work is of the order of magnitude of few decimeters. This scale is the same order of magnitude of the wavelength of the Sentinel-1 C band images used. RMSH is evaluated from a previously detrended surface [41] in order to separate multi-scale effects, with the remaining random roughness representing spatial variations [40, 51].

Considering that beach topography is highly heterogeneous in space, a local adaptation of the RMSH, the *loc*RMSH (local RMSH) index has been applied in the present work. A sliding window calculates the local variations in random roughness. The choice of an appropriate window size is crucial for capturing different surface patterns [51]. The local RMSH is obtained by the following equation [52]:

$$locRMSH = \sqrt{\frac{1}{N}\sum_{n=1}^{N} \mid z_n \mid^2} \quad (1)$$

with:

- *loc*RMSH, local root-mean squared height;
- N the number of points in each cell;
- z_n, the z-value at the n-th points in the window;

In the analysis of the present work, the local adaptation of the RMSH will be used. It will be referred to it as RMSH.

3.2.1. Choice of the window size: comparison between High Resolution and Low Resolution dataset

The selected area was scanned with the above specifications continuously during two years. To investigate the effect of the relatively low resolution (LR) of this data set on the RMSH evaluation, the same area was scanned with higher resolution (HR) and these data have been compared to the LR data acquired one hour later in order to define the window cell size for the *loc*RMSH estimation. The same laser scanner with 0.015 ° angular spacing was used on two occasions to acquire a scan of the same area resulting in a point density of about 43 points/m^2 and the same footprint size (see Table 1). This leads to more overlapping footprints.

Preprints (www.preprints.org) | NOT PEER-REVIEWED | Posted: 28 January 2022 doi:10.20944/preprints202201.0434.v1

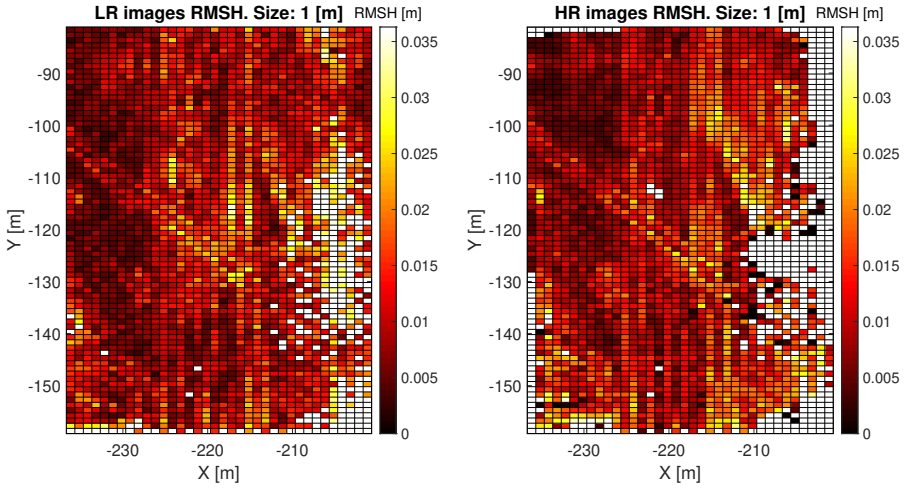

Figure 5. median RMSH evaluated for each pixel with 1m window size; comparison between HR and LR. The diagonal feature in the middle is a result of tire tracks from bulldozers crossing the study site.

Table 1. Properties of the data set from permanent laser scanning used in this study. LR and HR data only differ in angular resolution, point density and number of files. Incidence angle, point density and footprint size are averaged over the study area. In the present study, HR data (two files) collected during two different days have been only used for a comparison with LR data in order to investigate the effect of the resolution on the RMSH evaluation.

Data set	LR	HR
Wavelength [nm]	1550	1550
Range accuracy at 150 m [m]	0.008	0.008
Angular resolution [°]	0.03	0.015
Incidence angle [°]	77	77
Point density [pt/m^2]	10	42
Footprint size [m^2]	0.066	0.066

When considering LR point clouds, the disadvantage of using a window size smaller than 1 m is the low number of points per pixel (less than 11) and that the mean ratio between HR and LR is high, especially when considering a 0.5 m cell. Figure 5 and Figure 6 show, for one of the two considered days of analysis, the value of the local RMSH [m] evaluated in each window cell, measuring 1 m and 5 m respectively, to give an indication of the order of magnitude of RMSH on the sandy area considered. Figure 7 shows the RMSH median relative difference between HR and LR images when considering different window size, for window size moving from 0.5 m to 12 m. This parameter has been computed as follows: for each pixel the relative difference between the *loc*RMSH computed by using the HR image ($locRMSH_{HR}$) and the one computed with LR image ($locRMSH_{LR}$), indicated by the symbol ε_{RMSH} has been evaluated with the equation:

$$\varepsilon_{RMSH} = \frac{\mid locRMSH_{HR} - locRMSH_{LR} \mid}{locRMSH_{HR}}. \quad (2)$$

Then the median value of ε_{RMSH} has been computed. So Figure 7 shows the median value of ε_{RMSH} as a function of the windows size for two point clouds, acquired in August 2019. Whilst a significant difference (35%) exists for small window size (0.5 m), this difference is almost halved for 1 m cells and converges for window cells $\geq$4 m, where the difference is about 2%. Therefore, the dimension of the SAR pixels (12 m x 20 m) has been used as a RMSH window cell size in the present study, with reduced influence of the laser scanner resolution.

Preprints (www.preprints.org) | NOT PEER-REVIEWED | Posted: 28 January 2022 doi:10.20944/preprints202201.0434.v1

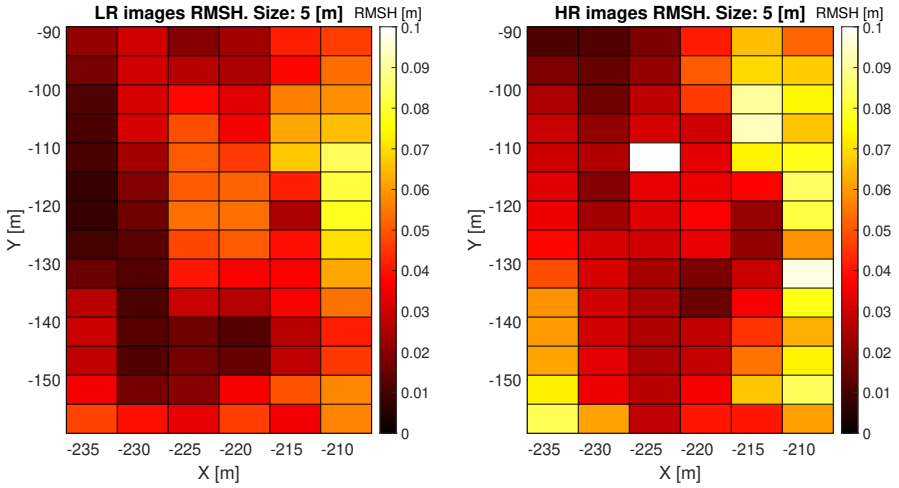

Figure 6. Median RMSH evaluated for each pixel with 5m window size; comparison between HR and LR.

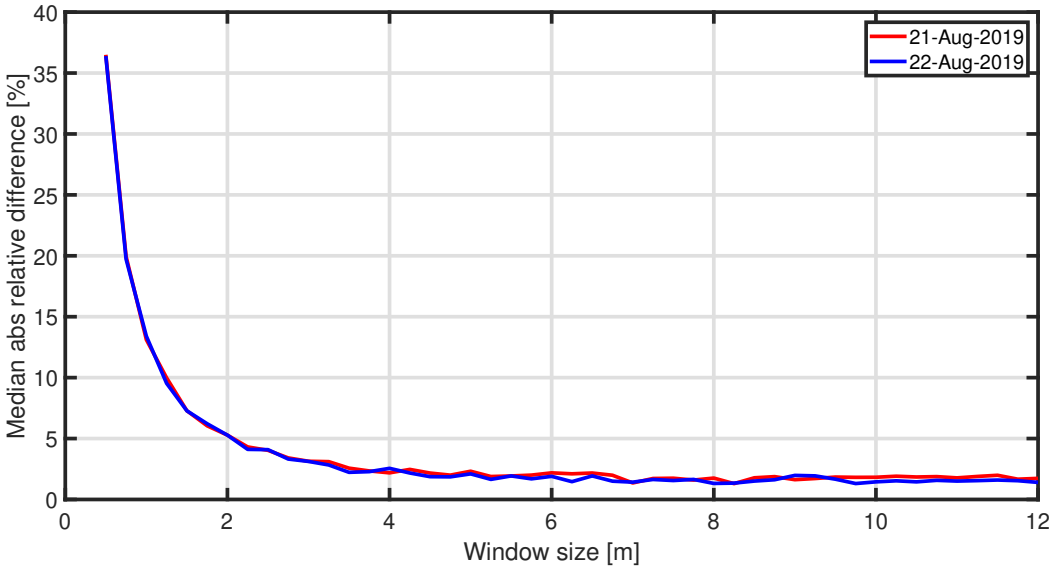

Figure 7. RMSH median relative difference between HR and LR images for the two analyzed days when considering different window size, for window size moving from 0.5 m to 12 m.

 doi:10.20944/preprints202201.0434.v1

3.3. PLS and SAR comparison

A total of 12 SAR pixels covers the study area as showed in Figure 2. All the presented analysis have been conducted for these 12 pixels. For this reason, considered PLS intensity values of points included in each pixel have been averaged. A correlation factor has been evaluated for each pixel of the study area between SAR backscatter and PLS intensity, averaged over time. Similar correlation factors have been retrieved when considering SAR VV and VH polarization in all the performed analysis. Therefore it has been decided to show in the rest of the present study only the results obtained with VV polarization.

In order to further investigate the correlation between SAR backscatter and PLS intensity, other variables which might affect the signal (both PLS and SAR) have been taken into consideration. For this purpose we consider wind speed and direction at the moment of the satellite pass and of the PLS scan of the beach. The wind speed has been considered separately for a first analysis: all the wind speeds values have been divided into three categories: low wind ($<4\,m/s$), medium wind ($4.1 - 8m/s$), high wind ($>8\,m/s$). The correlation factor between PLS intensity and SAR backscatter data set has been evaluated now for each pixel in the three cases of low, medium and high wind speed respectively.

4. Results

In this Section, we present the results of the present work in terms of correlation between SAR backscatter and PLS intensity, see Section 4.1. The influence of weather phenomena - in terms of wind conditions - and of the surface roughness on the PLS intensity and on the correlation between PLS intensity and SAR backscatter is further analysed in Section 4.2 and 4.3 respectively.

4.1. PLS and SAR correlation

The correlation factor between PLS intensity and SAR backscatter (VV polarization) evaluated for each pixel of the study area is shown in Figure 8: a generally positive but low correlation between the two variables in each pixel exists. Wind speed and direction at the moment of the satellite pass and of the PLS scan of the beach have been considered to further investigate the correlation between SAR and PLS signals. The correlation factor between PLS intensity and SAR backscatter (VV polarization) data has been evaluated now for each pixel in the three cases of low, medium and high wind speed respectively (see Figure 9). Compared to the previous analysis, the correlation between SAR and PLS data in the separate categories is now always higher and positive for each pixel when considering low or medium wind (up to 0.5 correlation factor). For high wind speed, the correlation becomes lower and irregular, both positive and negative depending on the considered pixel. To further define the correlation values, also the wind directions have been considered. The correlation factor has been evaluated for different sectors corresponding to different wind directions: each sector ranges 90° (see Figure 10). In Figure 10, each sector represents a 90° wind direction section and each of the 12 rings represents a row of pixel starting from pixel 1, which is located on the sea-side (inner ring) and moving towards pixel 12 (external ring), which is located on the city-side of the study area. It is noticed that the correlation has a interesting dependence on the wind direction and different directions show different correlations. In particular when the wind direction ranges 90°- 270°, several pixels show positive correlation of up to 0.6. For offshore wind (direction ranging between 210° and 360°), most of the pixels have negative correlation up to 0.4. Most of the sectors have similar range of colors, meaning that the 12 pixels of the study area present similar correlation on equal wind direction conditions.

4.2. Weather data effect

A separate analysis has been conducted on the PLS data in order to evaluate to what extent the weather phenomena affect its intensity. In the present study, the same stack of data used in the previous analysis collected during 88 days (acquired between 19/08/2019 and 22/04/2021) has been analyzed. During this period, only six days presented an accu-

Preprints (www.preprints.org) | NOT PEER-REVIEWED | Posted: 28 January 2022 doi:10.20944/preprints202201.0434.v1

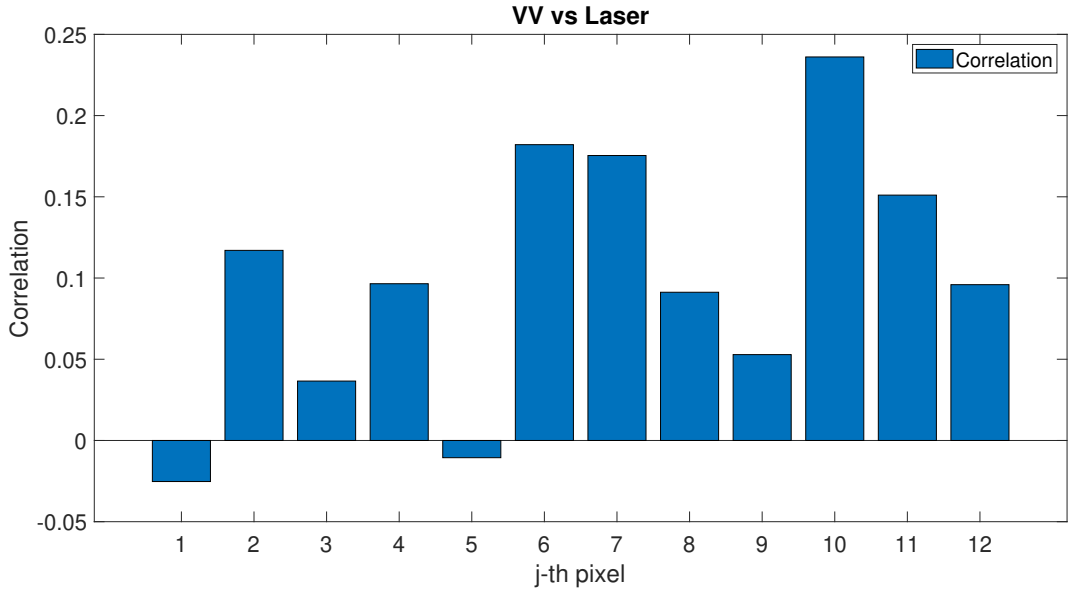

Figure 8. Correlation factor between SAR (VV polarization) backscatter and PLS intensity evaluated for each pixel of the study area.

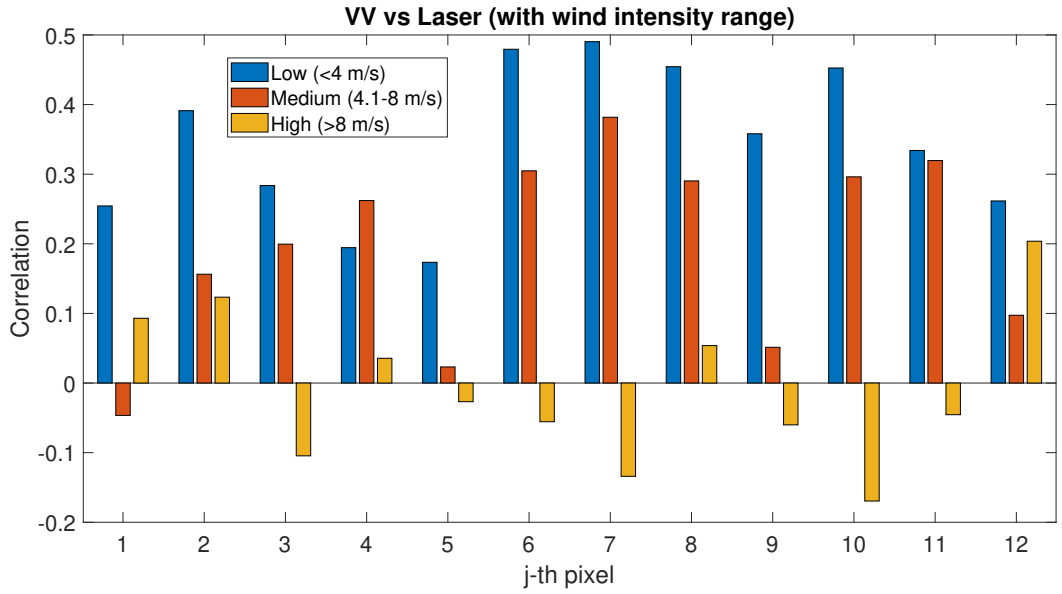

Figure 9. Correlation factor between PLS intensity and SAR (VV polarization) backscatter evaluated for low, medium and high wind speed conditions.

Preprints (www.preprints.org) | NOT PEER-REVIEWED | Posted: 28 January 2022 doi:10.20944/preprints202201.0434.v1

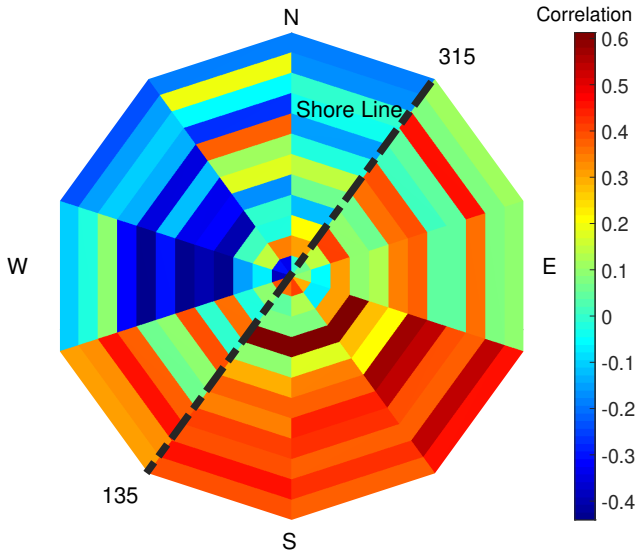

Figure 10. Correlation factor (colorbar) between PLS intensity and SAR backscatter evaluated for different overlapping sectors ranging 90° wind directions. In the figure, each sector represents a 90° wind direction section and each of the 12 rings represents a row of pixel starting from pixel 1, which is located on the sea-side (inner ring) and moving towards pixel 12 (external ring), which is located on the city-side of the study area. The dotted black line represents the orientation of the shore line in Noordwijk.

mulation precipitation bigger than 0 mm/h. These days were considered not sufficient for the statistic analysis. Therefore only analysis on the influence of wind has been performed.

At first, the wind speed has been considered. Figure 11 shows the correlation factor between PLS intensity and wind speed for low, medium and high wind speed condition, compare Section 3.3. For low and medium wind, each pixel shows that the PLS intensity decreases with increasing wind. For high wind speed, the correlation turns positive and ranges for each pixel between 0.6 and 0.8. This change of sign in the correlation factor between PLS signal and high wind speed condition could explain the lack of correlation between PLS and SAR data, as shown in Figure 9. The wind direction has also been considered and the correlation factor between PLS intensity and SAR backscatter has been evaluated for each pixel and for each wind direction section (See Figure 12). As in the previous section, the correlation factor has been evaluated for different overlapping sectors ranging 90° wind directions. In the figure, each sector represents a 90° wind direction section and each of the 12 rings represent a row of pixel starting from pixel 1, which is located on the sea-side (inner ring) and moving towards pixel 12 (external ring), which is located on the city-side of the study area. Again, certain directions show different correlation: in particular, the correlation factor between PLS and wind speed is negative for almost all pixels (up to 0.5) for wind directions ranging between 90° and 300° (mostly onshore wind), whilst a positive correlation exists (up to 0.5) for mostly offshore wind (directions ranging 210° and 360°).

4.3. Roughness influence

The roughness variable and to what extent it affects both PLS intensity and SAR signal has been analyzed by comparing RMSH index with TLS and SAR data set respectively. As mentioned in Section 3.2, the RMSH index has been used as an indication of the roughness of the soil. The index has been locally evaluated for each pixel. As a first step, the correlation between the roughness and the wind has been evaluated (See Figure 13). As explained in Section 3.3, the correlation factor has been evaluated separately for low, medium and high wind speed. For low wind speed condition, the correlation with RMSH is negative

Preprints (www.preprints.org) | NOT PEER-REVIEWED | Posted: 28 January 2022 doi:10.20944/preprints202201.0434.v1

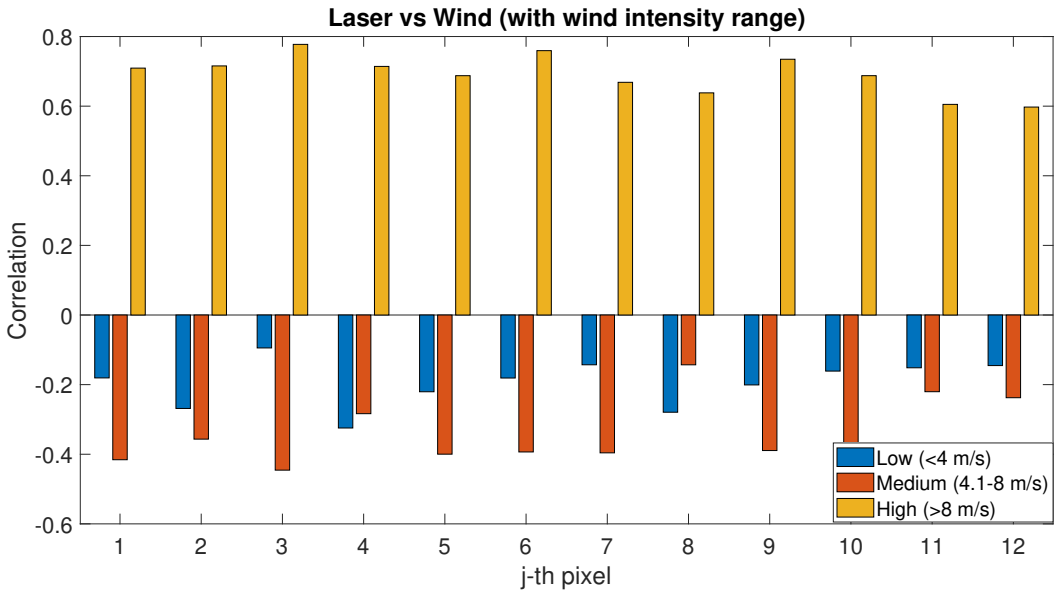

Figure 11. Correlation factor between PLS intensity and wind speed evaluated for low, medium and high wind speed conditions.

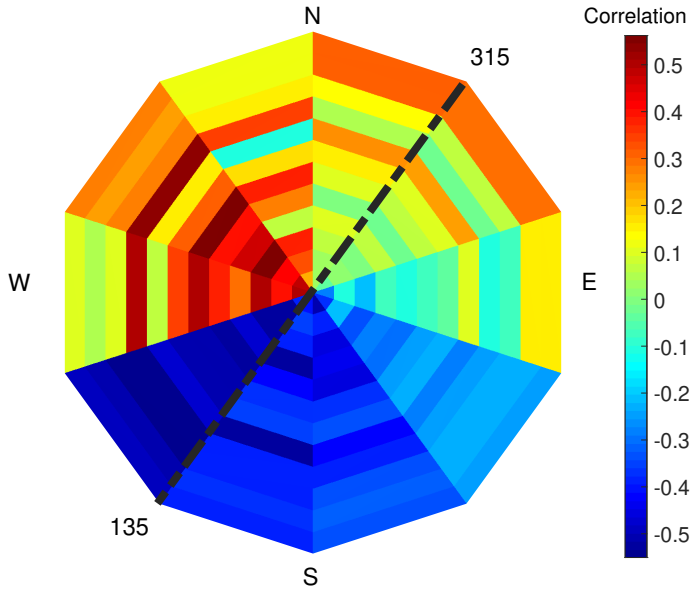

Figure 12. Correlation factor (colorbar) between PLS intensity and wind direction evaluated for different overlapping sectors ranging 90° wind directions. In the figure, each sector represents a 90° wind direction section and each of the 12 rings represent a row of pixels starting from pixel 1, which is located on the sea-side (inner ring) and moving towards pixel 12 (external ring), which is located on the city-side of the study area. The dotted black line represents the orientation of the shore line in Noordwijk.

Preprints (www.preprints.org) | NOT PEER-REVIEWED | Posted: 28 January 2022 doi:10.20944/preprints202201.0434.v1

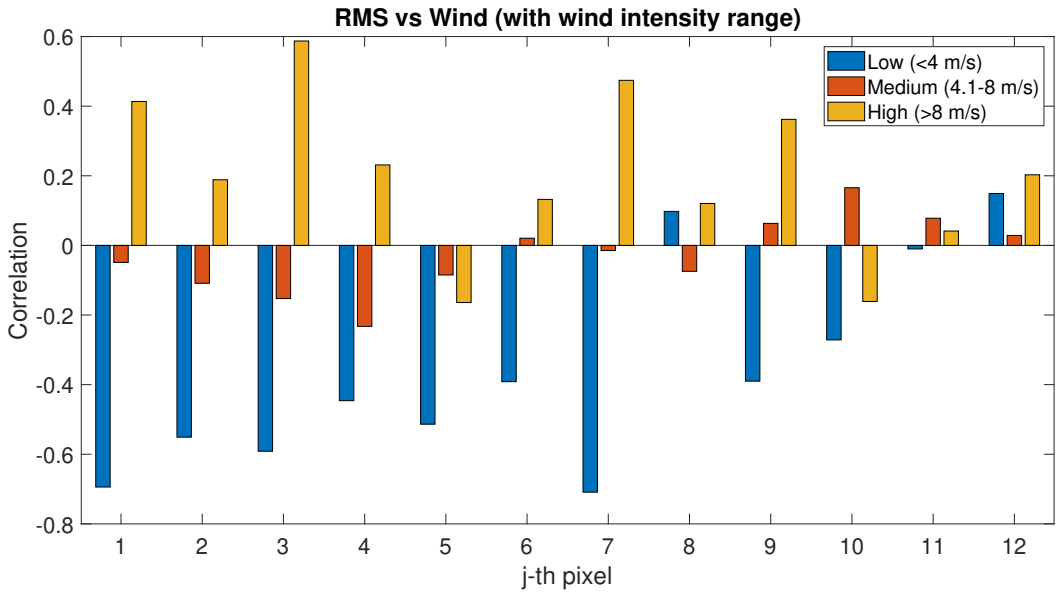

Figure 13. Correlation factor between RMSH and wind speed evaluated for low, medium and high wind speed conditions.

for almost all the pixels (up to 0.8); with increasing wind, the RMSH diminishes (lower roughness). For high wind speed most of the pixels show positive correlation with RMSH (higher roughness).

When considering the wind direction, see Figure 14, no significant correlation seems to exist between wind speed and RMSH, except for a slightly more regular positive correlation in the sectors ranging 90°-270°, where there also seems to be a more homogeneous behavior for the 12 pixels of the area when considering specific wind direction. For other directions, the correlation value is very variable for each considered pixel.

The RMSH values have been now compared with PLS intensity and their correlation has been evaluated for low, medium and high wind speed (See Figure 15). Excluding a few cases of high wind conditions for certain pixels, in particular pixels located on the city-side of the study area, a interesting positive correlation exists between PLS intensity and RMSH for each wind speed in all the pixels. In particular, for low wind condition the correlation is always positive; the cases of negative correlation are limited to a few pixels and to medium-high wind conditions.

The following analysis shows the comparison between SAR signal (VV polarization) and RMSH index for each pixel (See Figure 16). In this analysis, no particular trend can be highlighted in the correlation between SAR and RMSH, which is in general low and very variable considering different pixels.

5. Discussion

As presented in Section 4, when environmental variables are not considered, SAR and PLS data seems to have a low correlation (see Figure 8). When considering wind speed in the evaluation of SAR backscatter and PLS intensity correlation, a positive correlation is noticed only for low and medium wind speed conditions; for stronger wind, no correlation can be noticed (see Figure 9). The PLS has a negative correlation with low and medium wind speed; for high wind speed the correlation is high and always positive for each pixel (see Figure 11). This phenomenon could be explained with the following hypothesis:

1. High wind speed could dry the sand and, as a consequence, the PLS intensity is higher (since low sand moisture values correspond to higher PLS intensity [10, 15]);
2. There is a relation with the activation of aeolian transport - above a certain wind speed - and the sand particles moving on the beach surface which could affect the

Preprints (www.preprints.org) | NOT PEER-REVIEWED | Posted: 28 January 2022 doi:10.20944/preprints202201.0434.v1

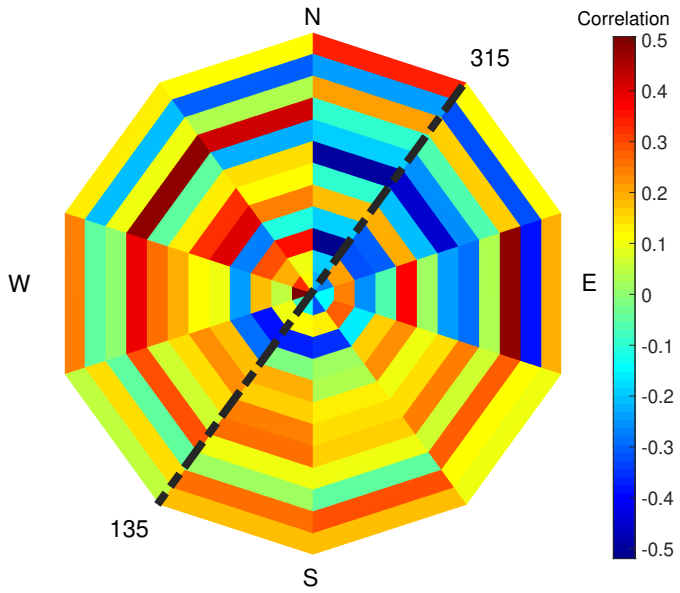

Figure 14. Correlation factor (colorbar) between RMSH and wind speed evaluated for different overlapping sectors ranging 90° wind directions. In the figure, each sector represents a 90° wind direction section and each of the 12 rings represents a row of pixel starting from pixel 1, which is located on the sea-side (inner ring) and moving towards pixel 12 (external ring), which is located on the city-side of the study area. The dotted black line represents the orientation of the shore line in Noordwijk.

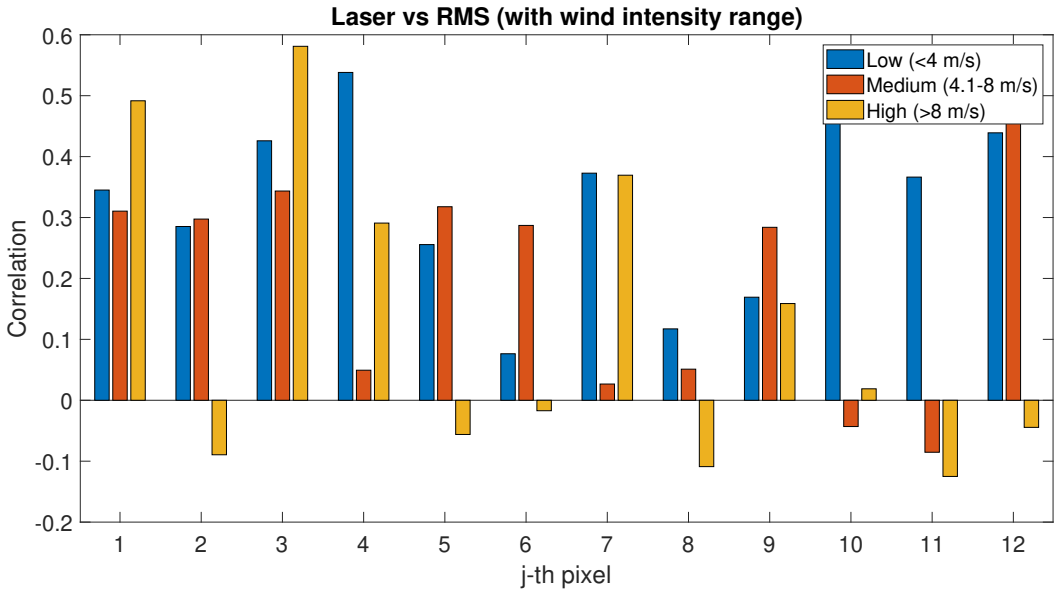

Figure 15. Correlation factor between PLS intensity and RMSH evaluated for low, medium and high wind speed conditions.

Preprints (www.preprints.org) | NOT PEER-REVIEWED | Posted: 28 January 2022 doi:10.20944/preprints202201.0434.v1

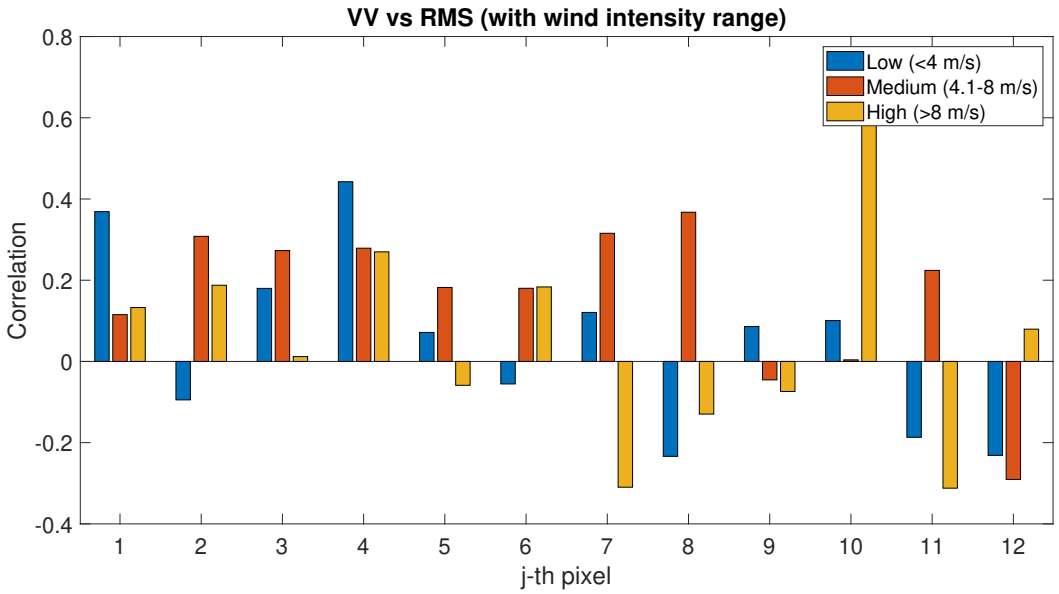

Figure 16. Correlation factor between SAR (VV polarization) and RMSH evaluated for low, medium and high wind speed conditions.

PLS intensity. In fact, the activation of aeolian transport requires wind speed above certain values [53].

The low correlation between SAR backscatter and PLS intensity for high wind speed can be ascribed to the correlation trend between PLS intensity and wind: when PLS has a negative correlation with wind speed (low and medium conditions), the behavior of its intensity is similar to the SAR backscatter; for high wind speed, PLS intensity behavior is reversed and it can no longer be compared to the SAR backscatter (compare Figures 9 and 11).
RMSH seems to have negative correlation with wind speed only for low wind condition: in this case, the effect of the wind is a reduction of the RMSH. For higher wind values, in particular for 4-8 m/s, no correlation can be noticed, see Figure 13. The hypothesis is that this phenomenon happens because wind speed in that range could produce a smoother profile on the sand surface.
Even if each pixel has a different correlation value, a positive correlation exists between RMSH and PLS intensity, in particular for low/medium wind speed (see Figure 15), whilst the correlation between SAR backscatter and RMSH is low but generally positive (see Figure 16). The hypothesis in this case is that this can be related to the order of magnitude of the RMSH values evaluated in the present work, which might not significantly affect the SAR wavelenght. For future studies, direction/orientation of the roughness, could be considered for determining a correlations with SAR data, as well as SAR systems with higher resolution with respect to Sentinel-1 which can be used and correlated to RMSH evaluated on different window size; roughness indices can be also evaluated on a lower order of magnitude to identify more specific correlations.

The correlation between PLS intensity and SAR backscatter shows specific wind directions where the correlation is particularly relevant. The same occurs for the correlation between PLS intensity and wind speed. The correlation between PLS intensity and wind speed, for low and medium wind speed, is negative; correlation between SAR backscatter and PLS intensity exists only when the correlation between PLS intensity and wind speed is negative. The wind direction where the correlation between PLS and wind speed is minimum (South) is the same than the direction where the correlation between SAR and PLS is maximum. South is also the direction where low and medium winds generally come from (compare Figures 3, 10 and 12).

 doi:10.20944/preprints202201.0434.v1

6. Conclusion

An investigation of the correlation between a permanently installed TLS and SAR systems has been conducted on the beach of Noordwijk: TLS data have been compared with simultaneously acquired Sentinel-1 SAR images. The correlation between TLS and SAR systems on sandy environments and the effect of environmental variables on their correlation have been analyzed for the first time. The wind both in terms of wind speed and direction has an impact on the correlation which could be further investigated, as well as the roughness which - at the scale used in the present work - did not show significant result but can be further analyzed on different scales to highlight more detailed information. The study showed that the correlation between the two considered systems when not considering external variables is positive but low (up to 0.25). When considering the wind speed, a higher correlation between TLS and SAR (up to 0.5) exists in the case of low and medium wind speed, whilst no particular correlation could be highlighted for high wind speed condition; a dependence on the considered pixel location of the study area has been noticed.

The wind direction has also been considered: for directions ranging 90°-270°, the entire area is homogeneous and there is a positive correlation between TLS and SAR up to 0.6, whilst for directions ranging 210°-360°, the correlation is negative up to 0.4. The correlation between TLS and wind has been separately considered with the following results: for low and medium wind, PLS and wind speed have a negative correlation whilst for high wind speed the correlation turns positive and ranges between 0.6 and 0.8. The correlation between TLS and wind speed also depends on the wind direction: for directions ranging 90°-300° a negative correlation is showed and for directions 210°-360° there is a positive correlation.

The influence of the surface roughness - evaluated in terms of RMSH - variable has been also considered, at first in terms of correlation between RMSH and wind. For low wind speed condition, the correlation between RMSH and wind is negative up to 0.8; the correlation gets positive (higher roughness) with the increase of the wind speed. No interesting correlation has been highlighted when considering the wind directions.

The analysis of the correlation between PLS and RMSH showed a positive correlation for each wind speed. In the analysis of the correlation between SAR and RMSH instead, no particular trend has been highlighted. In conclusion, this preliminary study allowed the individuation of a first range of conditions where TLS and SAR data present a good correlation. A better knowledge of the scenarios where the correlation between TLS and SAR is applicable, and of the extent of the existing correlation, could allow the exploitation of the combined use of TLS and SAR advantages, moving from the small scale (TLS) to a world-wide scale (SAR).

Author Contributions: The analysis has been conceived and designed by the three authors. VDB and MK collected the data and contributed data and analysis tools. VD performed the analysis presented in the results and wrote the paper. MK and RL critically reviewed the draft. RL supervised the work.

Funding: For the present work, VDB was supported by Mitsubishi Electric Corporation via the project Detecting, Identifying, and Classifying Sandy Soils using Satellite SAR Data. MK has been supported by the Netherlands Organization for Scientific Research (NWO, grant no. 16352) as part of the Open Technology Programme and by Rijkswaterstaat (Dutch Ministry of Infrastructure and Water Management).

Institutional Review Board Statement: Not applicable

Informed Consent Statement: Not applicable

Data Availability Statement: Not applicable

Acknowledgments: The authors would like to thank Grand Hotel Huis ter Duin for their cooperation and Sander Vos for his contribution to the data collection and maintenance of the PLS system.

Conflicts of Interest: The authors declare no conflict of interest.

References

(1) Danson, F. M.; Hetherington, D.; Morsdorf, F.; Koetz, B.; Allgower, B. *IEEE Geoscience and remote sensing letters* **2007**, *4*, 157–160.

(2) Eysn, L.; Pfeifer, N.; Ressl, C.; Hollaus, M.; Grafl, A.; Morsdorf, F. *Remote Sensing* **2013**, *5*, 5424–5448.

(3) Liang, X.; Kankare, V.; Hyyppä, J.; Wang, Y.; Kukko, A.; Haggrén, H.; Yu, X.; Kaartinen, H.; Jaakkola, A.; Guan, F., et al. *ISPRS Journal of Photogrammetry and Remote Sensing* **2016**, *115*, 63–77.

(4) Heritage, G.; Hetherington, D. *Earth Surface Processes and Landforms: The Journal of the British Geomorphological Research Group* **2007**, *32*, 66–74.

(5) Brasington, J.; Vericat, D.; Rychkov, I. *Water Resources Research* **2012**, *48*.

(6) Abellán, A.; Calvet, J.; Vilaplana, J. M.; Blanchard, J. *Geomorphology* **2010**, *119*, 162–171.

(7) Brodu, N.; Lague, D. *ISPRS Journal of Photogrammetry and Remote Sensing* **2012**, *68*, 121–134.

(8) Zelaya Wziątek, D.; Terefenko, P.; Kurylczyk, A. *Remote Sensing* **2019**, *11*, 2666.

(9) French, J.; Burningham, H. *Progress in Physical Geography* **2009**, *33*, 117–129.

(10) Di Biase, V.; Hanssen, R. F.; Vos, S. E. *Remote Sensing* **2021**, *13*, 1645.

(11) Lindenbergh, R. C.; Soudarissanane, S. S.; De Vries, S.; Gorte, B. G.; De Schipper, M. A. *The Photogrammetric Record* **2011**, *26*, 384–399.

(12) Dos Santos, A. L. S.; Amaro, V. E.; Santos, M. S. T. In MST: Rome, Italy, 12–13 June, 2014; Vol. Proceedings of the 7th International Terrestrial Laser Scanner User Meeting.

(13) Nield, J. M.; King, J.; Jacobs, B. *Aeolian Research* **2014**, *12*, 9–17.

(14) Nield, J. M.; Wiggs, G. F.; Squirrell, R. S. *Earth Surface Processes and Landforms* **2011**, *36*, 513–522.

(15) Smit, Y.; Ruessink, G.; Brakenhoff, L. B.; Donker, J. J. *Aeolian Research* **2018**, *31*, 19–27.

(16) Jin, J.; Verbeurgt, J.; De Sloover, L.; Stal, C.; Deruyter, G.; Montreuil, A.-L.; Vos, S.; De Maeyer, P.; De Wulf, A. *Isprs Journal of Photogrammetry and Remote Sensing* **2021**, *173*, 195–208.

(17) Tan, K.; Chen, J.; Zhang, W.; Liu, K.; Tao, P.; Cheng, X. *ISPRS Journal of Photogrammetry and Remote Sensing* **2020**, *159*, 129–139.

(18) Ruessink, G.; Brakenhoff, L.; van Maarseveen, M. In *EGU General Assembly Conference Abstracts*, 2014, p 2797.

(19) Nadal-Romero, E.; Revuelto, J.; Errea, P.; López-Moreno, J. *Soil* **2015**, *1*, 561–573.

(20) Luijendijk, A.; Hagenaars, G.; Ranasinghe, R.; Baart, F.; Donchyts, G.; Aarninkhof, S. *Scientific reports* **2018**, *8*, 1–11.

(21) Şekertekin, A.; Marangoz, A. M.; Abdikan, S. *International Journal of Environment and Geoinformatics* **2018**, *5*, 178–188.

(22) Baghdadi, N.; King, C.; Chanzy, A.; Wigneron, J.-P. *International Journal of Remote Sensing* **2002**, *23*, 4325–4340.

(23) Gorrab, A.; Zribi, M.; Baghdadi, N.; Mougenot, B.; Chabaane, Z. L. *Remote Sensing* **2015**, *7*, 747–766.

(24) Fung, A.; Liu, W.; Chen, K.; Tsay, M. *Journal of Electromagnetic Waves and Applications* **2002**, *16*, 689–702.

(25) Attarzadeh, R.; Amini, J.; Notarnicola, C.; Greifeneder, F. *Remote Sensing* **2018**, *10*, 1285.

(26) Philipp, M. B.; Levick, S. R. *Remote Sensing* **2020**, *12*, 49.

(27) Kaasalainen, S.; Hyyppä, J.; Karjalainen, M.; Krooks, A.; Lyytikäinen-Saarenmaa, P.; Holopainen, M.; Jaakkola, A., *Comparison of terrestrial laser scanner and synthetic aperture radar data in the study of forest defoliation*; na: 2010.

(28) Odipo, V. O.; Nickless, A.; Berger, C.; Baade, J.; Urbazaev, M.; Walther, C.; Schmullius, C. *Forests* **2016**, *7*, 294.

(29) Vos, S.; Lindenbergh, R.; de Vries, S.; Aagaard, T.; Deigaard, R.; Fuhrman, D. In *Coastal Dynamics*, 2017; Vol. 233.

(30) Kuschnerus, M.; Lindenbergh, R.; Vos, S. *Earth Surface Dynamics* **2021**, *9*, 89–103.

(31) Torres, R.; Snoeij, P.; Geudtner, D.; Bibby, D.; Davidson, M.; Attema, E.; Potin, P.; Rommen, B.; Floury, N.; Brown, M., et al. *Remote Sensing of Environment* **2012**, *120*, 9–24.

(32) Ulaby, F. T.; Batlivala, P. P. *IEEE Transactions on Geoscience Electronics* **1976**, *14*, 81–93.

(33) Ulaby, F. T. *Rader remote sensing and surface scattering and emission theory* **1982**, 848–902.

(34) Di Biase, V.; Hanssen, R. F. *Remote Sensing* **2021**, *13*, 4208.

(35) Lane, S. N. *Earth Surface Processes and Landforms* **2005**, *30*, 251–253.
(36) Govers, G.; Takken, I.; Helming, K. *Agronomie* **2000**, *20*, 131–146.
(37) Jester, W.; Klik, A. *Catena* **2005**, *64*, 174–192.
(38) Hugenholtz, C. H.; Brown, O. W.; Barchyn, T. E. *Aeolian Research* **2013**, *10*, 161–169.
(39) Barneveld, R. J.; Seeger, M.; Maalen-Johansen, I. *Earth Surface Processes and Landforms* **2013**, *38*, 90–94.
(40) Milenković, M.; Pfeifer, N.; Glira, P. *Remote Sensing* **2015**, *7*, 2007–2045.
(41) Van Wesemael, B.; Poesen, J.; de Figueiredo, T.; Govers, G. *Earth Surface Processes and Landforms* **1996**, *21*, 399–411.
(42) Huang, C.-h.; Bradford, J. M. *Soil Science Society of America Journal* **1992**, *56*, 14–21.
(43) RIEGL Data Sheet, RIEGL VZ-2000 http://www.riegl.com/uploads/tx_pxpriegldownloads/RIEGL_VZ-2000i_Datasheet_2019-11-22.pdf.
(44) Tan, K.; Chen, J.; Qian, W.; Zhang, W.; Shen, F.; Cheng, X. *Remote Sensing* **2019**, *11*, 331.
(45) RIEGL Data Sheet, RIEGL VZ-2000.
(46) Cutter, M.; Eves, S.; Remedios, J.; Humpage, N.; Hall, D.; Regan, A. In *Proceedings of ESA Living Planet Symposium ESA SP-722*, 2013, pp 2146–13.
(47) European Space Agency, E. S. A. Copernicus Open Access Hub (https://scihub.copernicus.eu/dhus/#/home) (accessed 12/30/2021).
(48) Veloso, A.; Mermoz, S.; Bouvet, A.; Le Toan, T.; Planells, M.; Dejoux, J.-F.; Ceschia, E. *Remote sensing of environment* **2017**, *199*, 415–426.
(49) European Space Agency, E. S. A. Sentinel-1 Toolbox (S1TBX) (http://step.esa.int/main/doc/tutorials/) (accessed 12/30/2021).
(50) Gulácsi, A.; Kovács, F. *Remote Sensing* **2020**, *12*, 1614.
(51) Haubrock, S.-N.; Kuhnert, M.; Chabrillat, S.; Güntner, A.; Kaufmann, H. *Catena* **2009**, *79*, 128–139.
(52) Daponte, P. *IEEE Std 181-2003* **2003**, 1–60.
(53) Van Rijn, L. *Coastal Engineering* **2022**, *171*, 104051.